Vortex Majorana braiding in a finite time

Thore Posske,[1] Ching-Kai Chiu,[2] and Michael Thorwart[1]
[1]*I. Institut für Theoretische Physik, Universität Hamburg, Jungiusstraße 9, 20355 Hamburg, Germany*
[2]*Kavli Institute for Theoretical Sciences, University of Chinese Academy of Sciences, Beijing 100190, China*

(Received 9 August 2019; revised manuscript received 17 April 2020; accepted 20 April 2020; published 21 May 2020)

Abrikosov vortices in Fe-based superconductors are a promising platform for hosting Majorana zero-energy modes. Their adiabatic exchange is a key ingredient for Majorana-based quantum computing. However, the adiabatic braiding process cannot be realized in state-of-the-art experiments. We propose to replace the infinitely slow, long-path braiding by a procedure that only slightly moves vortices in a special geometry without actually physically exchanging the Majoranas, like a Majorana carousel. Although the resulting finite-time gate is not topologically protected, it is robust against variations in material-specific parameters and in the braiding speed. We prove this analytically. Our results carry over to Y junctions of Majorana wires.

DOI: 10.1103/PhysRevResearch.2.023205

I. INTRODUCTION

Recent experiments on low-dimensional superconducting structures have revealed localized electronic states at the Fermi level. Although still debated, these states can be attributed to "half-fermionic" exotic electronic states, the Majorana zero modes. Spatially isolated Majorana zero modes are not lifted from zero energy when coupled to ordinary quasiparticles and are a key ingredient for demonstrating nonuniversal topological quantum computing [1–4], despite some susceptibility to external noise [5,6]. Majorana modes have supposedly been detected at the ends of semiconducting wires [7,8] and designed atomic chains with helical magnetic structures [9] and, in particular, at the surface of superconductors with a superficial Dirac cone, e.g., Fe-based superconductors. There, Abrikosov vortices carry spatially localized peaks in the density of states at zero bias voltage [10–19]. We call the latter vortex Majoranas.

The next milestone towards topological quantum computing as well as the final evidence of Majorana zero modes is to achieve Majorana braiding, i.e., moving two Majorana zero modes around each other adiabatically [2,4,20–24]. This naive implementation of Majorana braiding in Fe-based superconductors poses major experimental problems despite the fundamental limitation that a true adiabatic evolution of perfectly degenerate levels cannot be achieved in principle. First, the length of the exchange path is on the order of micrometers such that braiding would take up to minutes in current setups, introducing high demands on sample quality, temperature, and experimental control for guaranteeing coherent transport of the vortex without intermediate quasiparticle poisoning [25]. Second, braiding the vortices results in twisted flux lines in the bulk of the Fe-based superconductor. This induces an energetic instability [26], hindering braiding and eventually causing relaxation events that disturb the zero-energy subspace and thereby quantum computation.

In this work, we substantially simplify the direct approach of physically braiding vortex Majoranas and show how braiding is realized in finite time. To this end, vortex Majoranas are spatially arranged such that changing the position of one of them on a short, well-defined path is equivalent to ordinary braiding. For current experimental systems like $FeTe_xSe_{1-x}$ [13,27–29], the allowed timescales for our braiding operation ranges from adiabatically slow up to nanoseconds. The protocol is robust against variations in material parameters and in the local speed of the vortex motion, which we prove by an analytical finite-time solution. Unwanted couplings that lift the degeneracy of the ground state are excluded by the special spatial arrangement of the vortices and are additionally exponentially suppressed on the Majorana superconducting coherence length ξ.

For our proposal, we presume that a reliable mechanism for moving vortices is available. Tremendous progress in this regard was recently made by moving vortices with the cantilever of a magnetic force microscope [25,30,31]. Additionally, the controlled nanoscale assembly of vortices was achieved with the heated tip of a scanning tunneling microscope (STM) [32] by letting the vortices follow the locally heat suppressed superconducting gap. Regarding our proposal, STM manipulation potentially has the advantage of simultaneously resolving the local density of states (LDOS). Eventually, positioning the vortices amounts to engineering the hybridization between Majorana modes. Therefore, the presented finite-time results carry over to Y junctions of Majorana wires [1,2,7,8], where the hybridization between the Majorana modes at the periphery and the center is altered [22,33–35].

The structure of this work is as follows. In Sec. II, we first introduce the general spatial geometry of vortex

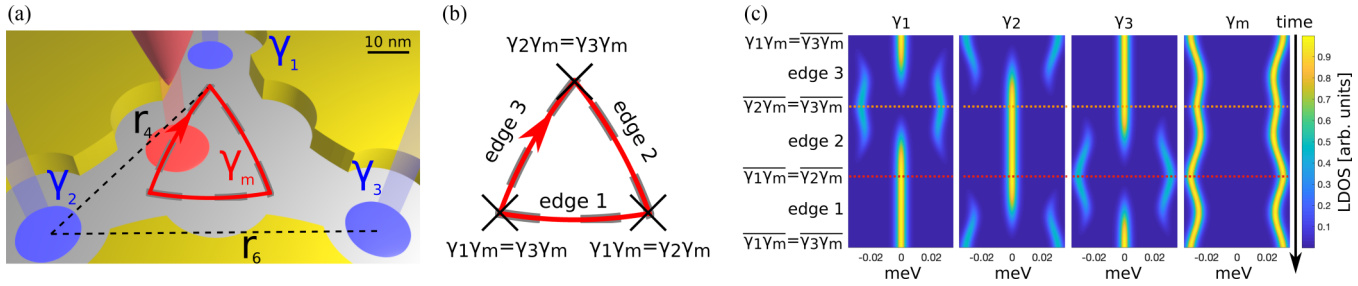

FIG. 1. (a) Setup: three decoupled vortex Majoranas γ_1, γ_2, γ_3 (blue) that are r_6 away from each other. A fourth, movable vortex Majorana γ_m (red) is on a path that is r_4 away from the exterior ones. (b) Path of γ_m to realize the braiding gate. (c) LDOS evolution for each vortex core as γ_m is moved. Two zero-bias peaks at exterior vortices and an energy splitting at the movable vortex are always present. The LDOS for each vortex does not break particle-hole symmetry significantly, supporting the validity of a low-energy model.

Majoranas that is needed to perform vortex Majorana braiding in finite time. The specific length scales of the geometry on $FeTe_xSe_{1-x}$ is derived by a realistic tight-binding model, which we introduce in Sec. III. In Sec. IV, we described the finite-time braiding protocol, which is based on moving one of the vortex Majoranas on a well-defined short path. The tight-binding model is used in combination with a low-energy model to show that the braiding gate is realized for special braiding times in a real system. To determine the robustness of the protocol against variations in material-specific parameters, we discuss an exact finite-time solution for a special set of parameters in Sec. V. The exact solution is connected to the numerical solutions of realistic models. In particular, we show that variations of material-specific parameters do not introduce errors in the braiding protocol if the total time for the braiding procedure is adjusted properly. Instead, the breaking of the C_3 symmetry of the structure and deviations from the perfect positions of the vortices can introduce errors in the braiding gate, which we estimate in Sec. IV. We conclude the discussion in Sec. VII.

II. SETUP

We consider three vortex Majoranas $\gamma_1, \gamma_2, \gamma_3$ at the corners of an equilateral triangle with a fourth, movable vortex Majorana γ_m near the center (see Fig. 1). A key element of the setup is that the distances between the vortices minimize the hybridization between the exterior vortex Majoranas. In a low-energy, long-distance continuum model, the hybridization strength of two vortex Majoranas [36,37] is proportional to $\cos(k_F r + \pi/4)e^{-r/\xi}/\sqrt{r}$, where r is the distance between their centers and k_F is the Fermi momentum. Two vortex Majoranas hence decouple at distances

$$r_j = \pi(j - 3/4)/k_F, \tag{1}$$

where j is a positive integer. The formula changes slightly for real systems and in the presence of multiple vortex Majoranas yet negligibly as far as our results are concerned. Furthermore, thermal fluctuations in the superconducting gap Δ, which in principle set an upper limit to the temperature [38], can be neglected in the regime of validity of Eq. (1), which does not depend on Δ. In the setup (Fig. 1), the exterior vortices are a distance r_6 away from each other, so that no hybridization takes place between them. The central vortex is moved along a path that is exactly r_4 away from at least one exterior vortex, as shown in Fig. 1(b). Finite-time Majorana braiding is realized by moving γ_m along this braiding path in a specified time T. The setup has C_3 symmetry and mirror symmetry, which we assume to hold in the following if not stated otherwise. Using r_4 and r_6 results in a particularly short braiding path on $FeTe_xSe_{1-x}$, where the superconducting Majorana coherence length is $\xi \approx 13.9$ nm. The direct distance between the exterior vortices is ~80 nm, and γ_m is never farther than ~6.5 nm away from the center. Other distances r_j can be used as well, in particular for different material systems.

III. REALISTIC TIGHT-BINDING MODEL FOR THE BRAIDING GATE

The distances given in Eq. (1), which describe when vortex Majoranas decouple, are derived from an approximation of the hybridization of exactly two vortex Majoranas. However, the structure at hand comprises four vortex Majoranas, so that any hybridization between two vortex Majoranas will unavoidably be affected by the presence of the remaining two. In addition, the presence of magnetic flux from additional vortices will alter the hybridization. Thus, we employ a more realistic tight-binding model for $FeTe_{0.55}Se_{0.45}$ [19] with four vortices for our theoretical calculation. This model captures the essence of the topological superconductivity in $FeTe_{0.55}Se_{0.45}$ by including a surface Dirac cone with real, material-specific parameters—its chemical potential $\mu = 5$ meV, the Fermi velocity of the Dirac cone $v_F = 25$ nm meV, and the Fermi momentum $k_F = \mu/v_F = 0.2$ nm^{-1}. Furthermore, we introduce an s-wave superconducting gap ($\Delta = 1.8$ meV) [15] to include superconductivity on the surface and add vortices carrying one magnetic flux quantum, obeying the London equations with a London penetration depth of $\lambda = 500$ nm [28,29]. In this setup, a vortex Majorana with zero energy arises at a vortex core on the surface of $FeTe_{0.55}Se_{0.45}$ [19]. Its characteristic length scales are given by the Majorana coherence length $\xi = v_F/\Delta = 13.9$ nm and the oscillation length of the Majorana hybridization $\pi/k_F = 15.7$ nm.

We insert four vortices into the tight-binding model for $FeTe_{0.55}Se_{0.45}$ to create the setup in Fig. 1(a). To find the correct positions, we start with the vortex distribution from the continuum model as shown in Fig. 2(a), with

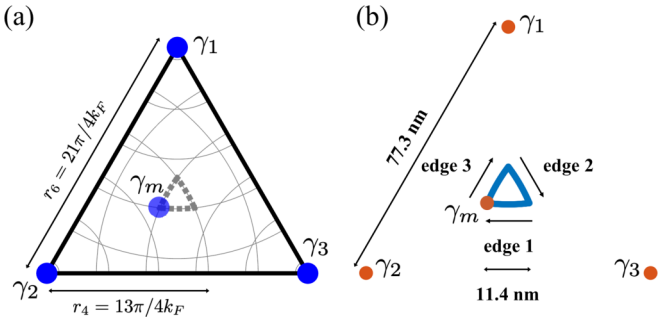

FIG. 2. (a) The vortex configuration for the setup of Fig. 1 in a long-distance continuum approximation [see Eq. (1)] and (b) the resulting material-specific length scales in the realistic tight-binding model.

$r_4 = 13\pi/(4k_F) = 51.1$ nm and $r_6 = 21\pi/(4k_F) = 82.5$ nm. These distances are iteratively adjusted until the final realistic values shown in Fig. 2(b) are obtained. For the ideal initial conditions, we need $iJ\gamma_2\gamma_\mathrm{m}$ to be the only hybridization present in the low-energy Hamiltonian at time $t = 0$,

$$H(0) = i(J\gamma_2 + a\gamma_1 + a\gamma_3)\gamma_\mathrm{m} + ib\gamma_3\gamma_1 + ic\gamma_2(\gamma_3 + \gamma_1), \tag{2}$$

whereas the residual hybridizations vanish. Since additional factors (e.g., magnetic flux, decay phase correction) influence the strength of the Majorana hybridization in the tight-binding model, the residual hybridizations generally do not exactly vanish. We find that, with a precision of 0.1 nm, an edge length of 77.3 nm and a distance $\overline{\gamma_2\gamma_\mathrm{m}} = 38.0$ nm are optimal. The minimal values of the residual hybridizations are $a/J = 0.3\%$, $b/J = 0.9\%$, and $c/J = 1.4\%$ [see Eq. (2)], which result from deviations from the ideal braiding path, the positions of exterior vortices, and other factors. We furthermore employ the tight-binding model to confirm that the residual Majorana hybridizations are not significantly increased during the passage of γ_m along the braiding path.

IV. BRAIDING PROTOCOL

In the following, we provide a step-by-step recipe for finite-time Majorana braiding using $FeTe_{0.55}Se_{0.45}$ as an exemplary platform. To this end, we employ a material-specific tight-binding model [19] (see Sec. III). We discuss the essential steps: (1) arranging the vortex positions, (2) calibrating the braiding path, (3) performing the braiding gate, and (4) reading out quantum states.

We first propose how to construct the setup shown in Fig. 1(a). Consider vortex Majoranas on the surface of $FeTe_{0.55}Se_{0.45}$. In the low-field regime $\leqslant 1$ T, the arrangement of the vortices is close to a triangular lattice [16], where the strength of the magnetic field controls the lattice constant. For the setup in Fig. 1(a), the tight-binding model predicts an ideal edge length of $r_6 = 77.3$ nm, corresponding to a magnetic field of 0.36 T. The concrete experimental value can be obtained by calibration relative to this starting point. A deviation of about 0.1 nm from the perfect positions does not crucially affect the protocol (see Sec. VI). We next use the aforementioned techniques [25,30–32] to move a vortex γ_m to the center of one Majorana triangle (γ_1, γ_2, γ_3) and isolate this formation by moving surrounding vortices away. Finally, we precisely adjust the positions of these four vortices such that only two zero-bias tunneling peaks appear at the positions of γ_1 and γ_3, while a small energy splitting of ~ 25 μeV is present at γ_2 and γ_m (see Fig. 1). Because of this energy splitting, we assume a temperature below 0.3 K for quantum information processing, which is achieved in state-of-the-art experiments.

For the braiding protocol, the braiding path, shown in Fig. 1(b), and the braiding time are important. We start by discussing the former. The braiding path is calibrated by ensuring that the LDOS for each vortex Majorana during the braiding process qualitatively aligns with the results shown in Fig. 1(c). Hence, initially, only γ_2 and γ_m hybridize, so that γ_1 and γ_3 exhibit zero-bias peaks. Furthermore, γ_3 always possesses a zero-bias peak during the first third of the braiding protocol. When γ_m moves towards γ_1, the energy splitting starts to transit from γ_2 to γ_1. The zero-bias peaks eventually appear at γ_2 and γ_3 when γ_m is closest to γ_1. In the remaining two thirds of the braiding path, the LDOS evolves as in the first third, but with suitably permuted indices of the vortex Majoranas [see Fig. 1(c)]. Importantly, two vortex Majoranas remain at zero energy throughout the whole braiding process. Furthermore, the energy splitting transits from γ_2 to γ_1 and then back to γ_3. On the other hand, the LDOS of γ_m never possesses any zero-bias peak, as shown in Fig. 1(c), since it always couples to another vortex Majorana. Observing the LDOS evolution for each vortex is the primary step to check successful braiding. To replace the technically demanding simultaneous measurement of the LDOS at each vortex, we first probe the LDOS at each vortex with an STM and then move the central vortex γ_m a short step along the braiding path. We iterate this procedure along the full braiding path until γ_m is back to the starting point.

We next have to confirm the informational change after braiding. The important data from the LDOS measurement to this end are the energy splitting and the peak heights of the vortex Majoranas that were collected in the previous step [see Fig. 1(c)]. From the energy splittings, a low-energy model can be derived that determines the braiding time, the resulting quantum gate operation on the degenerate ground state, and its quality. The model is explained in greater detail below. Braiding is then experimentally realized by moving γ_m along the previously saved braiding path in the calculated braiding time without probing any LDOS.

Finally, reading out the change in the quantum state after braiding is an important task, which was discussed previously. In particular, the Majorana qubit can be read out either by measuring the resonant current in Coulomb blocked systems [39], where charge fluctuations are suppressed and quantum information is thus protected, or by interferometry [40–42]. Importantly, Majorana braiding and readout are distinct processes, such that the readout time is not limited to happen on the timescale of the braiding.

Next, we describe how the protocol is implemented with the realistic tight-binding model and show in what respect the results are robust against material parameter changes by connecting the numerical solution to an analytic one.

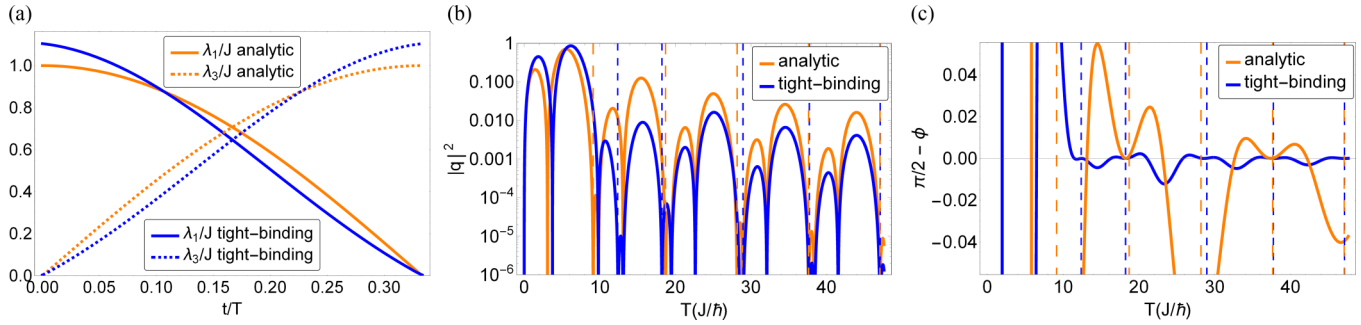

FIG. 3. Realization of the braiding gate. Realistic tight-binding parameters (blue) and analytically solvable parameters (orange) when γ_m is moved along the braiding path in the time T. (a) Hybridization strengths λ_1 and λ_3 ($\lambda_2 = 0$ not shown) during the first third of the braiding process. (b) Unwanted excitations $|q|^2$ vanish around specific times T_n, Eq. (6) (vertical dashed lines), for realistic as well as analytically solvable parameters. The zeros are protected. (c) When the quasiparticle excitations vanish at the dashed lines, the finite-time Berry phase ϕ reaches the perfect adiabatic braiding value of $\pi/2$.

V. BRAIDING: VALIDATION AND QUALITY

To validate that Majorana braiding is realized for vanishing residual couplings a, b, and c [see Eq. (2)], we consider the time-dependent low-energy Hamiltonian

$$H(t) = iJ[\lambda_1(t)\gamma_1 + \lambda_2(t)\gamma_2 + \lambda_3(t)\gamma_3]\gamma_m, \tag{3}$$

which describes the Majorana modes with energies much smaller than that of the Caroli–de Gennes–Matricon (CdGM) states [12,13]. All γ_j obey the Majorana algebra [1], $|\lambda_i(t)| \leqslant 1$ are time-dependent functions describing the hybridization strengths, and $J \approx 25\ \mu$eV (for our setup on $FeTe_{0.55}Se_{0.45}$) is the maximal hybridization energy of two Majoranas. Having used the distances from Eq. (1) in between most vortices, additional Majorana hybridizations are excluded. Similar Hamiltonians have been studied in the adiabatic limit [10,33,34] and with projective measurements [22,35] in setups for superconducting wires. The distinguishing features of our work are that we employ a time-dependent Hamiltonian and consider an experimentally realistic example system. Braiding on the timescale of gigahertz would tremendously outperform infinitely slow braiding.

It can be shown directly that the braiding protocol works in the adiabatic regime. By the definition of the braiding path and as shown in Fig. 1(c), one of the $\lambda_i(t)$ vanishes while two of the $\lambda_i(t)$ vanish at the corners of the triangle. The vector $\boldsymbol{\lambda}(t) = (\lambda_1(t), \lambda_2(t), \lambda_3(t))$ therefore encloses a spherical angle of $\pi/2$ after the braiding protocol. In the adiabatic limit, the time evolution hence converges (up to a phase) to the braiding operator [33,34,41,43,44] $\lim_{T\to\infty} U(T) \propto 1 - \gamma_1\gamma_2 \propto B_{1,2}$.

To describe the nonadiabatic regime, we fit the low-energy parameters of Eq. (3) to the realistic tight-binding model [see Fig. 3(a)], allowing us to employ explicit Runge-Kutta methods for the numerical simulation of the time evolution. Because we assume C_3 and mirror symmetries to hold during the braiding process, we symmetrize the tight-binding data accordingly. Deviations from these symmetries can introduce errors (see Sec. VI). To show that Majorana braiding is realized, we use two indicators. These are the amount of quasiparticle excitations $|q|^2$ and the phase difference ϕ between ground states of different parities. In particular, $|q|^2$ is the probability of leaving the degenerate ground state by the finite-time manipulation of the vortex positions, and the phase ϕ is an extension of the Berry phase to finite-time processes. We neglect other sources of quasiparticle excitations, assuming a temperature below 0.3 K, as stated above. As shown in Figs. 3(b) and 3(c), we find that the quasiparticle excitations $|q|^2$ and the deviation of the finite-time Berry phase ϕ from $\pi/2$ vanish simultaneously at times T_n. Therefore, perfect finite-time braiding is achieved at times T_n without physically braiding vortex Majoranas. In $FeTe_xSe_{1-x}$ the corresponding timescales are larger than 0.24 ns. This timescale is much slower than the timescale corresponding to excitations of CdGM states $\hbar E_F/\Delta^2 \approx 3.33$ ps, where Δ is the size of the superconducting gap and E_F is the Fermi energy.

The braiding protocol could be susceptible to variations in material parameters or the local speed of γ_m. In the following, we prove that these deviations are irrelevant by analytically solving a time-dependent Hamiltonian. We also find numerically that quasiparticle excitations stemming from slightly misplaced vortices are insignificant (see Sec. VI).

If the time-dependent hybridization strengths along edge 3 in Fig. 1(b) take the form

$$\lambda_1(t) = \sin\left(\frac{3\pi t}{2T}\right), \quad \lambda_2(t) = \cos\left(\frac{3\pi t}{2T}\right), \quad \lambda_3(t) = 0, \tag{4}$$

the time evolution along edge 3 can analytically be given as $U_{2,1}$, where

$$U_{j,k}(t) = e^{-\gamma_j\gamma_k\frac{3\pi t}{4T}} e^{\gamma_j\gamma_m\frac{Jt}{\hbar} + \gamma_j\gamma_k\frac{3\pi t}{4T}}. \tag{5}$$

That Eq. (5) is the solution of the Schrödinger equation is verified in the Appendix. The solution is obtained by a rotating-wave ansatz and by solving a time-independent differential equation. Notably, the exact time evolution of Eq. (5) is equivalent to adiabatic braiding $U_{i,j}(T_n) = B_{i,j}$ at times

$$T_n = 3\pi\sqrt{n^2 - 1/16}\,\hbar/J, \tag{6}$$

where n is a positive integer. The time evolution for moving γ_m along all three edges is $U(T) = U_{3,2}(T)U_{1,3}(T)U_{2,1}(T)$. Hence, $U(T_n) \propto B_{1,3}$. The analytic model therefore realizes analytically proved perfect braiding by moving γ_m along a short path in finite time.

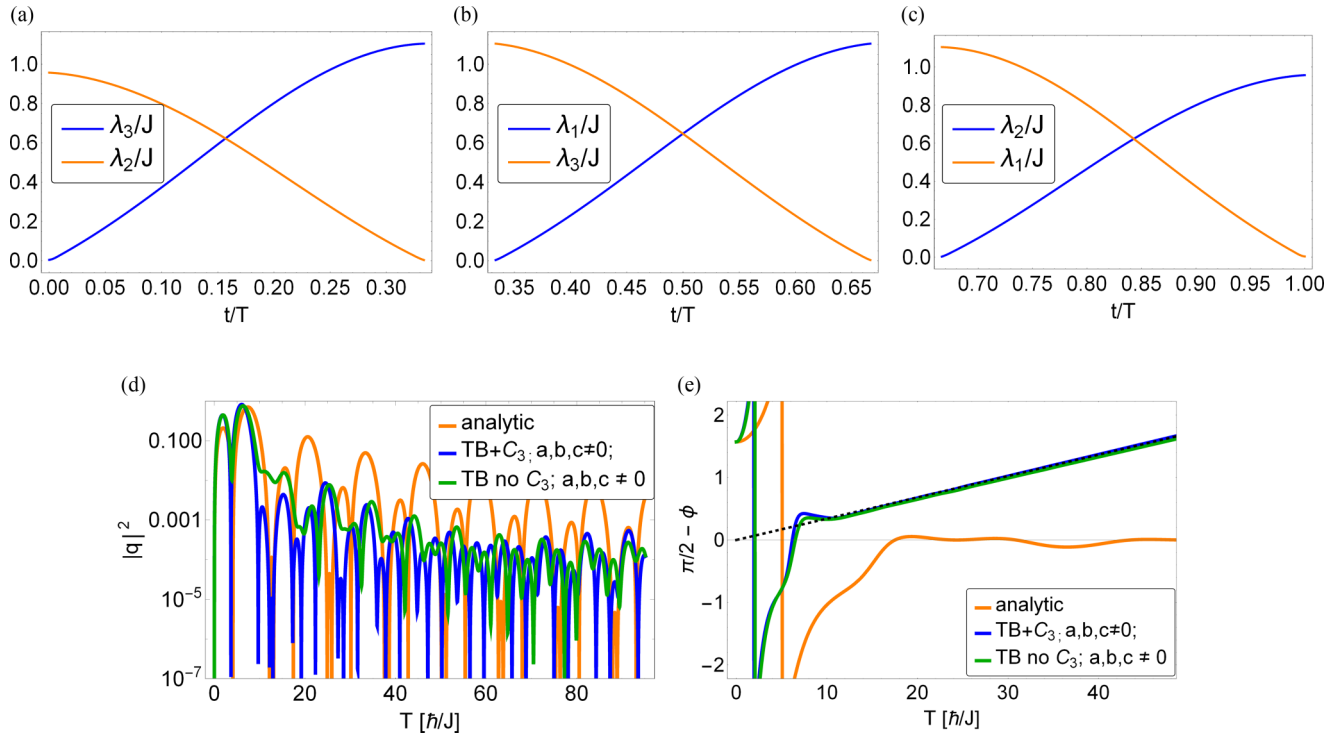

FIG. 4. (a)–(c) Realistic time-dependent hybridizations that break the C_3 symmetry, extracted from the tight-binding model (edge 3 to edge 1, from left to right). In each plot, the omitted coupling constant is close to zero. Bottom: Realization of the braiding gate with additional realistic residual couplings (blue, numerical) and a broken C_3 symmetry (green, numerical). The couplings are $a/J = 0.3\%$, $b/J = 0.9\%$, and $c/J = 1.4\%$ [see Sec. III and Eq. (2)]. For comparison, the analytic curves (orange) of Fig. 3 are included. (d) Unwanted quasiparticle excitations $|q|^2$. For a lifted ground-state degeneracy (blue curve) there are times T for which the unwanted quasiparticle excitations vanish. For an additionally broken C_3 symmetry (green curve), the formerly protected zeros lift. (e) Finite-time Berry phase ϕ as defined in the main text. Since the ground state is no longer degenerate, an additional dynamic phase additionally appears, which increases the adiabatic Berry phase of $\pi/2$ (blue and green curves). The additional dynamic phase is approximately linear in time (asymptotic black dashed line).

We next consider the case where γ_m is on edge 3 and the hybridizations $\lambda_1(t)$ and $\lambda_2(t)$ differ from the analytic solution but still keep $\lambda_3(t) = 0$. This is the case for the realistic tight-binding model. The general time evolution that respects mirror and C_3 symmetries is $U^g_{2,1}$, with

$$U^g_{j,k}(T) = b_1(T) + b_2(T)\gamma_j\gamma_m + b_3(T)\gamma_m\gamma_k + b_4(T)\gamma_k\gamma_j, \tag{7}$$

where $b_i(T)$ are real coefficients. Additional terms are excluded by the reduced number of Majorana hybridizations and by mirror symmetry. The complete time evolution operator along all three edges is

$$U^g(T) = U^g(T)_{3,2}U^g(T)_{1,3}U^g(T)_{2,1}. \tag{8}$$

The probability to excite quasiparticles after a full passage of γ_m along the braiding path is $|q^g|^2$, with

$$\begin{aligned} q^g(T) &= \mathrm{Tr}\{(\gamma_1 + i\gamma_2)(\gamma_3 + i\gamma_m)U^g(T)\}/4 \\ &= \sqrt{2}e^{\frac{i\pi}{4}}[b_4(T) - b_1(T)]\{1 - [\Sigma_i b_i(T)]^2\}. \end{aligned} \tag{9}$$

The number of quasiparticle excitations is hence given by a product of real polynomials. For example, the analytical model of Eq. (4) results in

$$q^a = e^{\frac{i\pi}{4}}\frac{\pi^3 \sin\left(\frac{\theta}{2}\right)}{2\theta^3}\left[\frac{J}{\hbar\omega}\frac{\theta}{2\pi}\sin(\theta) - \cos(\theta) - \frac{J^2}{\hbar^2\omega^2}\right], \tag{10}$$

with $\theta = \pi\sqrt{J^2 + \hbar^2\omega^2}/(\hbar\omega)$ and $\omega = 3\pi/(4T)$. At times T_n [see Eq. (6)] and additional transcendental times, the quasiparticle excitations $|q^a|^2$ hence vanish. In real systems, q generally differs from the analytical solution but remains a product of the real polynomials $b_1 - b_4$ and $1 - (\sum_i b_i)^2$, each of which is continuously connected to its counterpart in the analytical solution. Single zeros of q are therefore shifted but not lifted by small deviations. Only large deviations eventually annihilate two zeros simultaneously. In particular, the low-energy model extracted from the realistic tight-binding calculations deviates significantly from the analytically solvable protocol [see Fig. 3(a)]. Yet the zeros of q persist and only shift slightly, as shown in Fig. 3(b).

To finally analytically verify perfect braiding, we consider the finite-time extension of the Berry phase given by the phase difference

$$\phi = \arg\{\langle 0|U^g|0\rangle/\langle 1|U^g|1\rangle\} \tag{11}$$

between the states $|0\rangle$ and $|1\rangle = (\gamma_2 - i\gamma_m)|0\rangle$. Here, $|0\rangle$ is defined by $(\gamma_2 + i\gamma_m)|0\rangle = 0$. In the adiabatic limit, ϕ equals the Berry phase, which is $\pi/2$ for Majorana braiding. We find that $\phi = \pi/2$, i.e., perfect braiding, at the zeros of q where $b_1(T) = b_4(T)$ in Eq. (10), as shown in Fig. 3(c). These are exactly the zeros corresponding to T_n in Eq. (6) in the analytical model.

VI. UNWANTED COUPLINGS AND BREAKING OF C_3 SYMMETRY

The proposed scheme is unexpectedly robust against variations in the residual couplings a, b, and c [see Eq. (2)] as long as the C_3 symmetry of the setup (see Fig. 1 of the main text) is maintained. In this section, we give numerical evidence of how unwanted quasiparticle excitations and deviations in the phase difference ϕ (see main text) emerge if the C_3 symmetry is slightly broken or if residual couplings are included that lift the degeneracy of the zero-energy subspace. To this end, we employ the protocol shown in Figs. 4(a)–4(c), which slightly breaks the C_3 symmetry, and incorporate the unwanted residual couplings $a/J = 0.3\%$, $b/J = 0.9\%$, and $c/J = 1.4\%$ [see Eq. (2)], which respect a 0.1-nm deviation from the perfect positions of the vortices.

As shown in Fig. 4(a), residual couplings are not increasing the unwanted quasiparticle excitations as long as the C_3 symmetry is not broken. Only breaking the C_3 symmetry results in additional quasiparticle poisoning, which can be suppressed to less than 10^{-6} by choosing the braiding time. Regarding the finite-time Berry phase, residual couplings introduce a time-dependent additional phase that needs to be compensated for [see Fig. 4(b)]. This additional dynamical phase is expected because unwanted couplings lift the ground-state degeneracy [43,44]. However, a deviation from the braiding phase of $\pi/2$ may turn out to be a merit and not a deficiency. Each zero of the unwanted quasiparticle excitations corresponds to the realization of another phase gate. This has the advantage that different braiding speeds realize different phase gates.

VII. CONCLUSION

We showed that Majorana braiding with superconducting vortices can be achieved robustly and in finite time by only slightly moving the vortices. The procedure avoids a long-time, incoherent, physical braiding process. We simulate the protocol in a realistic, material-specific tight-binding model and prove its robustness against variations of material parameters and a nonconstant braiding speed by an analytically solvable time-dependent model. Perfect braiding without physically braiding Majoranas therefore becomes possible in systems where the superconducting coherence length at the surface ξ is comparable to the Fermi wavelength. This requirement is met by $FeTe_xSe_{1-x}$. If ξ is much larger, controlled vortex manipulation becomes impractical, whereas if ξ is much smaller, the Majorana hybridizations fall below current experimental resolution. The finite-time braiding ultimately relies on tuning the coupling between Majorana modes. Therefore, the scheme can also be realized in Y junctions of 1D topological superconductors or by inserting and moving magnetic or nonmagnetic adatoms in between vortex Majoranas. Alternatively, the positions of anomalous vortices carrying Majorana modes [45] could directly be manipulated.

ACKNOWLEDGMENTS

We thank B. Bauer, T. Hanaguri, L. Kong, D.-F. Wang, and R. Wiesendanger for helpful discussions. T.P. and M.T. acknowledge support from the German Research Foundation Cluster of Excellence "Advanced Imaging of Matter" of the Universität Hamburg (DFG EXC 2056, Project No. 390715994). C.-K.C. is supported by the Strategic Priority Research Program of the Chinese Academy of Sciences (Grant No. XDB28000000).

APPENDIX: VERIFICATION OF THE ANALYTIC SOLUTION

In Eq. (5), we give the closed form of the time evolution corresponding to the Hamiltonian Eq. (3) with the time-dependent hybridizations of Eq. (4). Here, we verify the solution. The time evolution operator is the solution of the Schrödinger equation

$$\partial_t U(t) = -i/\hbar H(t) U(t), \tag{A1}$$

which is obtained from the usual form of the Schrödinger equation $\partial_t \Psi(t) = -i\hbar H(t)\Psi(t)$ by replacing $\Psi(t) = U(t)\Psi(0)$. Here,

$$H(t) = 2iJ\left[\cos\left(\frac{3\pi t}{2T}\right)\gamma_3 + \sin\left(\frac{3\pi t}{2T}\right)\gamma_1\right]\gamma_{\mathrm{m}}. \tag{A2}$$

The solution to Eq. (A1) can be found by a rotating-wave ansatz and the subsequent solution of a simpler differential equation. The result is

$$\begin{aligned} U(t) &= e^{-\gamma_3\gamma_1\frac{3\pi t}{4T}} e^{\gamma_3\gamma_{\mathrm{m}} Jt/\hbar + \gamma_3\gamma_1\frac{3\pi t}{4T}} \\ &= e^{-\omega t\gamma_3\gamma_1} e^{(J/\hbar)t\gamma_3\gamma_{\mathrm{m}} + \omega t\gamma_3\gamma_1} \\ &= [\cos(\omega t) - \gamma_3\gamma_1 \sin(\omega t)] \\ &\quad \times \{\cos(\alpha t) + t\,\mathrm{sinc}(\alpha t)[(J/\hbar)\gamma_3\gamma_{\mathrm{m}} + \omega\gamma_3\gamma_1]\}, \end{aligned} \tag{A3}$$

with $\omega = 3\pi/(4T)$ and $\alpha = \sqrt{\omega^2 + (J/\hbar)^2}$. To obtain the final form, we have used the algebra of the Majorana operators. The calculation can be verified using the fact that the parity sectors decouple, and $e^{i a \boldsymbol{n}\boldsymbol{\sigma}} = \cos(a) + i\boldsymbol{n}\boldsymbol{\sigma}\sin(a)$, where $\boldsymbol{\sigma} = (\sigma_1, \sigma_2, \sigma_3)$ is a vector containing all Pauli matrices and $\boldsymbol{n}$ is a vector of length 1.

Next, we verify the solution given above and in the main text by using a specific (faithful) representation of the operators, namely,

$$\gamma_1 = \frac{1}{2}\begin{pmatrix} 0 & 0 & 1 & 0 \\ 0 & 0 & 0 & 1 \\ 1 & 0 & 0 & 0 \\ 0 & 1 & 0 & 0 \end{pmatrix}, \quad \gamma_2 = \frac{1}{2i}\begin{pmatrix} 0 & 0 & 1 & 0 \\ 0 & 0 & 0 & 1 \\ -1 & 0 & 0 & 0 \\ 0 & -1 & 0 & 0 \end{pmatrix}, \tag{A4}$$

$$\gamma_3 = \frac{1}{2}\begin{pmatrix} 0 & 1 & 0 & 0 \\ 1 & 0 & 0 & 0 \\ 0 & 0 & 0 & -1 \\ 0 & 0 & -1 & 0 \end{pmatrix}, \quad \gamma_{\mathrm{m}} = \frac{1}{2i}\begin{pmatrix} 0 & 1 & 0 & 0 \\ 1 & 0 & 0 & 0 \\ 0 & 0 & 0 & -1 \\ 0 & 0 & -1 & 0 \end{pmatrix}. \tag{A5}$$

We insert Eq. (A3) into Eq. (A1) and find that the matrix representation of both sides of the resulting equation are the same. Explicitly, it is

$$[-i/\hbar H(t)U(t)]_{j,k} = i(J/\hbar)A_{j,k}(t)$$

and

$$[\partial_t U(t)]_{j,k} = i(J/\hbar)A_{j,k}(t).$$

Here,

$$\begin{aligned}
A_{1,1}(t) &= \cos(\alpha t)\cos(\omega t) \\
&\quad + t\,\mathrm{sinc}(\alpha t)[i(J/\hbar)\cos(\omega t) - \omega\sin(\omega t)], \\
A_{2,2}(t) &= \cos(\omega t)[i(J/\hbar)t\,\mathrm{sinc}(\alpha t) - \cos(\omega t)] \\
&\quad + \omega t\,\mathrm{sinc}(\alpha t)\sin(\omega t), \\
A_{4,1}(t) &= \cos(\alpha t)\sin(\omega t) \\
&\quad + t\,\mathrm{sinc}(\alpha t)[i(J/\hbar)\sin(\omega t) + \omega\cos(\omega t)], \\
A_{1,4}(t) &= \cos(\alpha t)\sin(\omega t) \\
&\quad + t\,\mathrm{sinc}(\alpha t)[-i(J/\hbar)\sin(\omega t) + \omega\cos(\omega t)], \\
A_{2,3}(t) &= -A_{4,1}(t),\ A_{3,2}(t) = -A_{1,4}(t), \\
A_{3,3}(t) &= A_{1,1}(t),\ A_{4,4}(t) = A_{2,2}(t).
\end{aligned}$$

Matrix elements that are not given vanish.

[1] A. Y. Kitaev, Phys. Usp. **44**, 131 (2001).
[2] J. Alicea, Y. Oreg, G. Refael, F. von Oppen, and M. P. A. Fisher, Nat. Phys. **7**, 412 (2011).
[3] S. R. Elliott and M. Franz, Rev. Mod. Phys. **87**, 137 (2015).
[4] C. Nayak, S. H. Simon, A. Stern, M. Freedman, and S. Das Sarma, Rev. Mod. Phys. **80**, 1083 (2008).
[5] J. C. Budich, S. Walter, and B. Trauzettel, Phys. Rev. B **85**, 121405(R) (2012).
[6] F. L. Pedrocchi and D. P. DiVincenzo, Phys. Rev. Lett. **115**, 120402 (2015).
[7] V. Mourik, K. Zuo, S. M. Frolov, S. R. Plissard, E. P. A. M. Bakkers, and L. P. Kouwenhoven, Science **336**, 1003 (2012).
[8] A. Das, Y. Ronen, Y. Most, Y. Oreg, M. Heiblum, and H. Shtrikman, Nat. Phys. **8**, 887 (2012).
[9] H. Kim, A. Palacio-Morales, T. Posske, L. Rózsa, K. Palotás, L. Szunyogh, M. Thorwart, and R. Wiesendanger, Sci. Adv. **4**, eaar5251 (2018).
[10] D. A. Ivanov, Phys. Rev. Lett. **86**, 268 (2001).
[11] L. Fu and C. L. Kane, Phys. Rev. Lett. **100**, 096407 (2008).
[12] D. Wang, L. Kong, P. Fan, H. Chen, S. Zhu, W. Liu, L. Cao, Y. Sun, S. Du, J. Schneeloch, R. Zhong, G. Gu, L. Fu, H. Ding, and H.-J. Gao, Science **362**, 333 (2018).
[13] J. X. Yin, Z. Wu, J. H. Wang, Z. Y. Ye, J. Gong, X. Y. Hou, L. Shan, A. Li, X. J. Liang, X. X. Wu, J. Li, C. S. Ting, Z. Q. Wang, J. P. Hu, P. H. Hor, H. Ding, and S. H. Pan, Nat. Phys. **11**, 543 (2015).
[14] Q. Liu, C. Chen, T. Zhang, R. Peng, Y.-J. Yan, C.-H.-P. Wen, X. Lou, Y.-L. Huang, J.-P. Tian, X.-L. Dong, G.-W. Wang, W.-C. Bao, Q.-H. Wang, Z.-P. Yin, Z.-X. Zhao, and D.-L. Feng, Phys. Rev. X **8**, 041056 (2018).
[15] P. Zhang, K. Yaji, T. Hashimoto, Y. Ota, T. Kondo, K. Okazaki, Z. Wang, J. Wen, G. D. Gu, H. Ding, and S. Shin, Science **360**, 182 (2018).
[16] T. Machida, Y. Sun, S. Pyon, S. Takeda, Y. Kohsaka, T. Hanaguri, T. Sasagawa, and T. Tamegai, Nat. Mater. **18**, 811 (2019).
[17] Y. Yuan, J. Pan, X. Wang, Y. Fang, C. Song, L. Wang, K. He, X. Ma, H. Zhang, F. Huang, W. Li, and Q.-K. Xue, Nat. Phys. **15**, 1046 (2019).
[18] S. Zhu, L. Kong, L. Cao, H. Chen, M. Papaj, S. Du, Y. Xing, W. Liu, D. Wang, C. Shen, F. Yang, J. Schneeloch, R. Zhong, G. Gu, L. Fu, Y.-Y. Zhang, H. Ding, and H.-J. Gao, Science **367**, 189 (2020).
[19] C.-K. Chiu, T. Machida, Y. Huang, T. Hanaguri, and F.-C. Zhang, Sci. Adv. **6**, eaay0443 (2020).
[20] T. Karzig, Y. Oreg, G. Refael, and M. H. Freedman, Phys. Rev. B **99**, 144521 (2019).
[21] T. Karzig, C. Knapp, R. M. Lutchyn, P. Bonderson, M. B. Hastings, C. Nayak, J. Alicea, K. Flensberg, S. Plugge, Y. Oreg, C. M. Marcus, and M. H. Freedman, Phys. Rev. B **95**, 235305 (2017).
[22] T. Karzig, Y. Oreg, G. Refael, and M. H. Freedman, Phys. Rev. X **6**, 031019 (2016).
[23] B. I. Halperin, Y. Oreg, A. Stern, G. Refael, J. Alicea, and F. von Oppen, Phys. Rev. B **85**, 144501 (2012).
[24] S. Vijay, T. H. Hsieh, and L. Fu, Phys. Rev. X **5**, 041038 (2015).
[25] B. H. November, J. D. Sau, J. R. Williams, and J. E. Hoffman, arXiv:1905.09792.
[26] I. Roy, S. Dutta, A. N. Roy Choudhury, S. Basistha, I. Maccari, S. Mandal, J. Jesudasan, V. Bagwe, C. Castellani, L. Benfatto, and P. Raychaudhuri, Phys. Rev. Lett. **122**, 047001 (2019).
[27] K. Jiang, X. Dai, and Z. Wang, Phys. Rev. X **9**, 011033 (2019).
[28] H. Kim, C. Martin, R. T. Gordon, M. A. Tanatar, J. Hu, B. Qian, Z. Q. Mao, R. Hu, C. Petrovic, N. Salovich, R. Giannetta, and R. Prozorov, Phys. Rev. B **81**, 180503(R) (2010).
[29] T. Klein, D. Braithwaite, A. Demuer, W. Knafo, G. Lapertot, C. Marcenat, P. Rodière, I. Sheikin, P. Strobel, A. Sulpice, and P. Toulemonde, Phys. Rev. B **82**, 184506 (2010).
[30] E. W. J. Straver, J. E. Hoffman, O. M. Auslaender, D. Rugar, and K. A. Moler, Appl. Phys. Lett. **93**, 172514 (2008).
[31] H. Polshyn, T. Naibert, and R. Budakian, Nano Lett. **19**, 5476 (2019).
[32] J.-Y. Ge, V. N. Gladilin, J. Tempere, C. Xue, J. T. Devreese, J. van de Vondel, Y. Zhou, and V. V. Moshchalkov, Nat. Commun. **7**, 13880 (2016).
[33] J. D. Sau, D. J. Clarke, and S. Tewari, Phys. Rev. B **84**, 094505 (2011).
[34] D. Meidan, T. Gur, and A. Romito, Phys. Rev. B **99**, 205101 (2019).
[35] S. Vijay and L. Fu, Phys. Rev. B **94**, 235446 (2016).
[36] M. Cheng, R. M. Lutchyn, V. Galitski, and S. Das Sarma, Phys. Rev. Lett. **103**, 107001 (2009).
[37] M. Cheng, R. M. Lutchyn, V. Galitski, and S. Das Sarma, Phys. Rev. B **82**, 094504 (2010).
[38] R. V. Mishmash, B. Bauer, F. von Oppen, and J. Alicea, Phys. Rev. B **101**, 075404 (2020).
[39] C.-X. Liu, D. E. Liu, F.-C. Zhang, and C.-K. Chiu, Phys. Rev. Appl. **12**, 054035 (2019).

[40] S. Plugge, A. Rasmussen, R. Egger, and K. Flensberg, New J. Phys. **19**, 012001 (2017).
[41] C.-K. Chiu, M. M. Vazifeh, and M. Franz, Europhys. Lett. **110**, 10001 (2015).
[42] D. Pekker, C.-Y. Hou, V. E. Manucharyan, and E. Demler, Phys. Rev. Lett. **111**, 107007 (2013).
[43] T. Kato, J. Phys. Soc. Jpn. **5**, 435 (1950).
[44] M. V. Berry, Proc. R Soc. A **392**, 45 (1984).
[45] P. Fan, F. Yang, G. Qian, H. Chen, Y.-Y. Zhang, G. Li, Z. Huang, Y. Xing, L. Kong, W. Liu, K. Jiang, C. Shen, S. Du, J. Schneeloch, R. Zhong, G. Gu, Z. Wang, H. Ding, and H.-J. Gao, arXiv:2001.07376.